Published in final edited form as:

Mol Cancer Ther. 2020 August ; 19(8): 1670–1681. doi:10.1158/1535-7163.MCT-20-0033.

Development of a MUC16-Targeted Near-Infrared Fluorescent Antibody Conjugate for Intraoperative Imaging of Pancreatic Cancer

Madeline T. Olson[a,b], **Nicholas E. Wojtynek**[a,b], **Geoffrey A. Talmon**[c,b], **Thomas C. Caffrey**[a,b], **Prakash Radhakrishnan**[a,b,c,e], **Quan P. Ly**[b,d], **Michael A. Hollingsworth**[a,b,c,e], **Aaron M. Mohs**[b,e,f,g]

[a]Eppley Institute for Research in Cancer and Allied Diseases, University of Nebraska Medical Center, Omaha, NE, 68198

[b]Fred and Pamela Buffett Cancer Cente, University of Nebraska Medical Center, Omaha, NE, 68198

[c]Department of Pathology and Microbiology, University of Nebraska Medical Center, Omaha, NE, 68198

[d]Department of Surgery, University of Nebraska Medical Center, Omaha, NE, 68198

[e]Department of Biochemistry and Molecular Biology, University of Nebraska Medical Center, Omaha, NE, 68198

[f]Department of Pharmaceutical Sciences, University of Nebraska Medical Center, Omaha, NE, 68198

[g]Center for Drug Delivery and Nanomedicine, University of Nebraska Medical Center, Omaha, NE, 68198

Abstract

Surgical resection is currently the only potentially curative option for patients with pancreatic cancer. However, the five-year survival rate after resection is only 25%, due in part to high rates of R1 resections, in which cells are left behind at the surgical margin, resulting in disease recurrence. Fluorescence-guided surgery (FGS) has emerged as a method to reduce incomplete resections and improve intraoperative assessment of cancer. Mucin-16 (MUC16), a protein biomarker highly

[*]**Correspondence to:** Aaron M. Mohs, Ph.D., Department of Pharmaceutical Sciences, Fred and Pamela Buffett Cancer Center, University of Nebraska Medical Center, 5.12.315 Scott Research Tower, Omaha, NE 68198-6858, aaron.mohs@unmc.edu.

AUTHORS' CONTRIBUTIONS

Conception and design: M.T. Olson, N.E. Wojtynek, P. Radhakrishnan, M.A. Hollingsworth, A.M. Mohs

Development of methodology: M.T. Olson, N.E. Wojtynek, A.M. Mohs

Acquisition of data: M.T.Olson, N.E. Wojtynek, Q.P. Ly, G.A. Talmon, Q.P. Ly, M.A. Hollingsworth, A.M. Mohs

Analysis and interpretation of data: M.T.Olson, N.E. Wojtynek, G.A. Talmon, A.M. Mohs

Writing, review and/or revision of the manuscript: M.T. Olson, N.E. Wojtynek, G.A. Talmon, Q.P. Ly, P. Radhakrishnan, M.A. Hollingsworth, A.M. Mohs

Administrative, technical or material support: T. Caffrey, A.M. Mohs

Study supervision: A.M. Mohs

Disclosure of Potential Conflicts of Interest

AMM is a co-inventor of image-guided surgery technology licensed to Spectropath, Inc. (Atlanta, GA). PR and MAH have equity interest in OncoCare Therapeutics, which has licensing rights to monoclonal antibody AR9.6.

overexpressed in pancreatic cancer, is a potential target for FGS. In this study, we developed a fluorescent MUC16-targeted antibody probe, AR9.6-IRDye800, for image-guided resection of pancreatic cancer. We demonstrated the efficacy of this probe to bind human pancreatic cancer cell lines *in vitro* and *in vivo*. In an orthotopic xenograft model, AR9.6-IRDye800 exhibited superior fluorescence enhancement of tumors and lower signal in critical background organs in comparison to a non-specific IgG control. The results of this study suggest that AR9.6-IRDye800 has potential for success as a probe for FGS in pancreatic cancer patients, and MUC16 is a feasible target for intraoperative imaging.

Keywords

Fluorescence-Guided Surgery; MUC16; Surgical Resection

INTRODUCTION

Pancreatic ductal adenocarcinoma (PDAC) remains a highly lethal and aggressive disease, characterized by its poor response to therapy, and advanced stage of disease at diagnosis. Surgical resection is currently the only curative option for patients with this disease (1,2). However, difficulties in differentiating between cancerous and non-cancerous tissue result in high rates of R1 resections, or resections with positive margin involvement, and thus high rates of recurrence (3,4). Pathological determination of resection status is defined by a minimum of a 1 mm tumor-cell free margin between the closest cancer cell and all resection margins to achieve a complete resection, or an R0 resection (5). Patients who undergo a complete R0 resection have improved survival compared to R1 resections, which exemplifies the importance of comprehensive intraoperative tumor detection and resection (6). While pre-operative imaging modalities play a critical role in initial staging, detection, and surgical planning, translating these images into an intraoperative setting can be challenging, leading to missed lesions (7). Thus, the 5-year survival rate for patients that undergo surgical resection is only approximately 25% (1). Fluorescence-guided surgery (FGS) has emerged as a method to reduce irradical resections, and improve intraoperative assessment of lesions (8). FGS relies on the preferential accumulation of a contrast agent in tumors, to differentiate malignant tissue from adjacent non-cancerous tissue with fluorescence. The implementation of FGS has the potential to improve outcomes of pancreatic cancer resections by improving the detection of the primary tumor, surgical margins, and residual disease (9). While FGS has clear potential for improving surgery in resectable cases, image guidance could also be employed to prevent unnecessary surgeries in unresectable cases, by highlighting metastatic lesions that have been missed in initial staging.

Near-infrared (NIR) dyes are preferentially employed for FGS because they exhibit low autofluorescence, reduced light scattering, and improved depth of penetration (10,11). These properties are critical, particularly in malignancies like pancreatic cancer, where the tumor is often deeply seated in the abdominal cavity. FGS systems required to visualize fluorophores intraoperatively have been extensively reviewed here (12). A wide variety of targeting vehicles have been developed preclinically and in clinical trials to direct contrast agents to

specific tumor targets, or tumor phenotypes, resulting in improved contrast agent specificity (13). Antibodies have been frequently used, particularly in clinical trials, because the high stability and target specificity, potentially low toxicity, and well-established conjugation strategies are favorable for probe development (14,15).

Current clinical trials in pancreatic cancer are investigating fluorescent antibody conjugates that target epidermal growth factor receptor (EGFR), vascular endothelial growth factor (VEGF-A), and carcinoembryonic antigen (CEA) for FGS (16,17). These initial clinical trials have demonstrated feasibility in delineating primary and metastatic disease. However, these studies also suggest the need to identify and expand alternative targeted probes to address the heterogeneity of biomarkers present in pancreatic tumors and improve intraoperative imaging (17). To address this problem, we investigated a new potential target for FGS in pancreatic cancer.

MUC16, also known as CA125, is overexpressed in 60–80% of pancreatic cancer (18). MUC16 is overexpressed in many different cancers, including colon, stomach, and esophageal, but has been most widely studied for its aberrant expression in ovarian cancer (18,19). Recent studies in pancreatic cancer have demonstrated that MUC16 expression is positively correlated to disease progression and poor prognosis (20,21). While MUC16 has shown promise as a prognostic and diagnostic biomarker for pancreatic cancer, it has not yet been investigated for FGS. Thus, the goal of this work was to develop a MUC16-targeted antibody probe that could achieve optimal delivery to identify pancreatic cancer intraoperatively with FGS. To achieve this, we utilized AR9.6, a monoclonal antibody (mAb) that targets isoforms of MUC16 (either fully glycosylated or aberrantly glycosylated). We hypothesized that targeting MUC16 with the AR9.6 fluorescent antibody probe would improve the detection of pancreatic cancer and provide strong contrast against surrounding tissue. In this study, we employ the antibody AR9.6, conjugated to the near infrared dye, IRDye800 to target pancreatic cancer. Our findings demonstrated strong fluorescence enhancement of pancreatic tumor xenografts with the AR9.6-IRDye800 probe and suggested the potential utility of this fluorescent probe for improved intraoperative imaging of pancreatic cancer.

MATERIALS AND METHODS

Antibody Conjugation

Mouse AR9.6 (Quest PharmaTech, Inc., Edmonton, Canada) and mouse IgG1 isotype (ThermoFisher Scientific, 02–6100; Waltham, MA) antibodies were reconstituted to 1 mg/ml in phosphate-buffered saline (PBS). A Zeba™ spin desalting column (ThermoFisher Scientific, 89891) was used to remove 0.1% sodium azide from the IgG1 antibody. 100 μl of 1M potassium phosphate was added to each mg of antibody to raise the pH to 8.5. IRDye800 N-hydroxysuccinimide (NHS) ester (0.5 mg, LI-COR Biosciences, 929–70020; Lincoln, NE) was dissolved in 50 μl of nanopure water, and vortexed briefly. 10 μl of the dye was added to 1 mg of antibody, and vortexed briefly to mix. Dye and antibody were incubated for 2 h at room temperature. Zeba™ spin desalting columns were used to remove excess dye, according to the instructions from the manufacturer. A 1 cm cuvette (Eppendorf, E0030106300; Hauppauge, NY) was loaded with a 1:10 dilution of the antibody in a 1:1

ratio of PBS and methanol. A Thermo Scientific Evolution 220 UV-visible spectrophotometer was used to determine dye: protein ratio (D/P), such that $\frac{D}{P} = \left[\frac{A_{780}}{\mathcal{E}_{Dye}}\right] \div \left[\frac{A_{280} - (0.03 \times A_{780})}{\mathcal{E}_{Protein}}\right]$, where $\mathcal{E}_{Dye}$ = 270,000 M^{-1} $cm^{-1}$and $\mathcal{E}_{Protein}$ = 203,000 M^{-1} cm^{-1}. The concentration of the antibody after conjugation was determined such that $\left(\frac{mg}{ml}\right) = \left[\frac{A_{280} - (0.03 \times A_{780})}{\mathcal{E}_{Protein}}\right] \times MW\ protein \times Dilution\ factor$. Conjugation resulted in an average of 3 dyes per antibody. The emission of the antibody conjugates was determined using a FluoroMax 4 spectrofluorometer (Horiba Scientific; Irvine, CA).

Cell Lines and Cell Culture

Pancreatic cancer cell lines acquired 2/2018 including HPNE (CVCL_C466), Colo357 (CVCL_0221), T3M4 (CVCL_4056), Capan1 (CVCL_0237), CFPAC (CVCL_1119), and HPAC (CVCL_3517) were obtained from Dr. Michael A. Hollingsworth, and OVCAR3 (CVCL_0465) cells acquired March 2018 were obtained from Dr. Adam R. Karpf. Cells were last tested for mycoplasma on March 21, 2018, using a PCR mycoplasma detection kit (ABM, G-238; Vancouver, CA). All cells were grown in RPMI 1640 (Corning, 10–040-CV; Tewksbury, MA), supplemented with 10% fetal bovine serum, 100 I.U. penicillin, and 100 μg/ml of streptomycin (P/S) (Corning, 30–002-CI). Cells were maintained at 37° C in a humidified incubator with 5% CO_2. In general, all cells were passaged fewer than 20 times, or one month after thawing before experimental use.

Western Blot

Cells were lysed with radioimmunoprecipitation assay (RIPA) buffer (ThermoFisher Scientific, 89900) supplemented with Halt protease inhibitor (ThermoFisher Scientific, 78440). 25 μg of protein were separated on a 4–15% polyacrylamide gel (Bio-Rad, 4568084; Hercules, CA) and transferred onto a nitrocellulose membrane (Bio-Rad, 1620115). The membrane was blocked with 5% Blotting-Grade Blocker (Bio-Rad, 170–6404) in TBST and incubated with AR9.6 (1:1000, 1mg/ml stock solution) and GAPDH antibody (1:2000, Cell Signaling Technology, 2118S; Danvers, MA) overnight at 4° C. The membrane was incubated with goat-anti mouse HRP secondary antibody (1:2000, Jackson Immunoresearch, 115–035-003; West Grove, PA), or goat-anti rabbit HRP secondary antibody (1:2000, Jackson Immunoresearch, 111–035-003) in 5% Blotting-Grade Blocker for 1 h on a rocker and was visualized with enhanced chemiluminescent (ECL) substrate (Bio-Rad, 1705060S).

For fluorescent western blotting, the membrane was blocked with 5% blotting grade blocking buffer in TBS. AR9.6-IRDye800 (1:5000 1mg/ml stock solution) and IgG-IRDye800 (1:2500 0.5 mg/ ml stock solution) were incubated with the membrane overnight at 4 °C in 5% blotting grade blocker in TBST. After washing, the membrane was incubated with goat anti-mouse IRDye800 (1:20,000, LI-COR Biosciences, 926–33210) in 5% blotting grade blocker in TBST, washed, and imaged on Odyssey CLx (LI-COR Biosciences).

Immunofluorescence

HPNE, Colo357, T3M4, and OVCAR3 cells were seeded at 30,000–40,000 cells per chamber of an 8 chamber slide (ThermoFisher Scientific, 154534), and allowed to adhere

overnight. Cells were washed 3x with 1X PBS and fixed in ice-cold methanol at −20° C for 20 min. After fixation, cells were washed with 1X PBS and blocked with 3% BSA in TBS for 1 h at room temperature. 5 μg/ml of AR9.6 and 5μg/ml of IgG1 were incubated with cells for 1 h at room temperature in 3% BSA in TBST. Cells were washed 3x with PBS. Fluoroshield mounting medium with 4′,6-diamidino-2-phenylindole (DAPI) (Abcam, ab104139; Cambridge, MA) was added to cover each chamber, and chambers were covered with a glass coverslip. Cells were imaged at 400X magnification on an Olympus DP80 Digital Camera and cellSens Dimension software.

Antibody Internalization

Colo357 cells were seeded as indicated above. Cells were incubated with AR9.6-IRDye800 for 1 hour at 37° C, followed by incubation with 60 nM of LysoTracker Deep Red (ThermoFisher Scientific, L12492) for 1 hour, and Hoescht nuclear stain (ThermoFisher Scientific, 62249) for 5 minutes. Cells were imaged as described above.

Animal Models

All animal work was performed under a protocol approved by the University of Nebraska Medical Center (UNMC) Institution of Animal Care and Use Committee (IACUC). Subcutaneous tumor models were generated by injecting 1×10^6 T3M4 or Colo357 cells suspended in 100 μl of 1:1 growth media and Matrigel (Corning, 356234) into the left flank of 6–8 week old female NU/J mice (Jackson Laboratories, 002019; Bar Harbor, ME). T3M4 tumors were allowed to grow for 11 days, and Colo357 tumors were allowed to grow for 30 days. Orthotopic tumor models were established by injecting 2.5×10^5 T3M4 cells suspended in 30 μl of PBS into the pancreas of 6–8 week old female NU/J mice as previously described (22). Surgery was conducted on a sterile drape, and a TP700 TPump Professional Core Warming and Cooling System (Stryker Corp; Kalamazoo, MI) maintained at 37° C. The surgical field was prepped by alternating swabs of povidone iodine and alcohol swabs. Mice were allowed to recover and were monitored after surgery. Buprenorphine (Bupranex®, Reckitt Benckiser Pharmaceuticals, 955531; Hull, England) (0.1 mg/kg) was administered twice per day for three days after surgery.

Fluorescence Imaging Dynamics

2 nmol of IRDye800 (free dye control, LI-COR Biosciences, 929–08972), IgG-IRDye800 isotype control or AR9.6-IRDye800 were injected via tail vein into female NU/J mice bearing subcutaneous tumors. Images were taken at 4, 24, 48, 72, 96, 120, and 144 h post-injection with the 800 nm channel and white channel on the Pearl® Trilogy small animal imaging system (LI-COR Biosciences). Full necropsies were performed at 144 h. Digestive organs were perfused with PBS, and all organs were imaged on the Pearl® Trilogy. Images were analyzed using Image Studio software version 5.0 (LI-COR Biosciences). Briefly, a region of interest (ROI) was drawn around the tumor, and a secondary ROI was drawn around the unaffected flank. Tumor to background ratios (TBR) were calculated as follows: (mean fluorescent signal in tumor / mean fluorescent signal in unaffected flank). Signal to noise ratios (SNR) were calculated as follows: (mean fluorescent signal in the tumor / standard deviation of the background)(23).

Fluorescence-Guided Surgery

T3M4 orthotopic tumors were implanted and allowed to proliferate for 20 days. Mice were injected with 1 nmol (based on dye) of AR9.6-IRDye800 or IgG-IRDye800 via tail vein injection. Mice were euthanized 144 h after antibody conjugate administration, and images were collected on the Pearl® Trilogy, Fluobeam 800 (Fluoptics; Cambridge, MA), and the Lab Flare RP1 (Curadel; Natick, MA) FGS systems. Tumor was resected with image guidance using the Fluobeam and Lab Flare imaging systems, and complete necropsies were subsequently conducted. AR9.6-IRDye800 and IgG-IRDye800 groups were resected using the same exposure time (500 ms). Fluobeam images were analyzed to calculate intraoperative TBR using Image J software (version 1.52a, NIH; Bethesda, MD). Briefly, intraoperative TBR (mean fluorescent signal in tumor/ mean fluorescent signal in normal pancreas or adjacent peritoneal tissue) was calculated by manually defining a ROI around the suspected tumor and adjacent background, and analyzing the mean signal in each identified region. Dissected organs were imaged on the Pearl® Trilogy. Organ signal was quantified with Image Studio software by manually defining ROI around each tissue and obtaining the mean fluorescent signal, and SNR was calculated as described above. Necropsied organs were spectrally analyzed using a wavelength-resolved semi-quantitative surgical detection system (24). The handheld probe was positioned 1cm above resected tissues. Points across the length of the tumor and pancreas were excited at 785 nm using 8 mW (low) laser power. Emission spectra were collected from 800–950 nm, consistent with previous reports (22,23)

Orthotopic Tumor Histology

Organs and tumors resected at 144 h after injection of antibody conjugates were embedded in optimal cutting temperature compound (OCT) blocks and stored at −20° C until processing for histology. Tissues were cut into 10 μm thick sections using a cryostat (Leica; Buffalo Grove, IL) and mounted on charged microscope slides (ThermoFisher, 22–037-246). Slides were dried at room temperature for 20 min and fixed with chilled acetone for 10 min, and allowed to dry at room temperature for 20 min. To detect the presence of AR9.6-IRDye800 or IgG-IRDye800 at 144 h, slides were imaged with an Olympus DP80 Digital Camera and cellSense Dimension Software in the FITC channel (tissue autofluorescence), and the 800 nm channel (AR9.6-IRDye800 or IgG-IRDye800). Hematoxylin and Eosin (H&E) staining was conducted according to standard procedures and imaged under brightfield microscopy.

Histology on Human Pancreatic Cancer Samples

Tumors resected at the time of surgery were flash-frozen and embedded in OCT. Immunohistochemistry was conducted using standard procedures for frozen tissues, and the AR9.6 antibody (1:125 dilution, 1 mg/ml stock solution). Tumors resected at autopsy were obtained from the University of Nebraska Medical Center’s Tissue Bank through the Rapid Autopsy Pancreatic (RAP) program in compliance with IRB 091–01. To ensure specimen quality, organs were harvested within three hours postmortem, and the specimens placed in formalin for immediate fixation. Sections were cut from paraffin blocks of formalin-fixed tissue into 4 micron thick sections and mounted on charged slides. Slides were stained with

OC125 (Roche, 760–2610; Basel, Switzerland) according to standard protocols for paraffin-embedded tissues. Slides were imaged on an Olympus DP80 Digital Camera and cellSense Dimension software.

Statistical Analysis

All statistical analyses were conducted using Graph Pad Prism software version 7.03 (GraphPad Software). 2-way ANOVA was used, followed by Tukey's test for multiple comparisons to compare differences in SNR and TBR between AR9.6-IRDye800, IgG-IRDye800, and unconjugated IRDye800. Multiple t-tests were used to compare the biodistribution of AR9.6-IRDye800 to IgG-IRDye800. The SNR of AR9.6-IRDye800 and IgG-IRDye800 were compared with an unpaired t-test. All values are reported as the mean ± standard deviation.

RESULTS

MUC16 in pancreatic cancer patients

MUC16 has been implicated as a potential target for pancreatic cancer. To investigate the expression of MUC16 in patients, immunohistochemistry was conducted on patient samples. Human pancreatic cancer samples shown in Figure 1A, 1B, and 1C were obtained from the UNMC rapid autopsy pancreas program, and samples shown in Figure 1D and 1E were collected during surgical resection. These specimens were stained for MUC16 expression with mAb AR9.6. All patient samples were analyzed by a board-certified pathologist (G.A.T). Normal pancreas samples obtained at surgery and autopsy and pancreatitis samples obtained at autopsy showed no expression of MUC16 (Figure 1A, 1B, 1E). Conversely, pancreatic cancer samples collected at autopsy showed strong positive apical staining as well as diffuse cytoplasmic and membrane staining of MUC16 (Figure 1C). Precursor lesions termed pancreatic intraepithelial neoplasms, or PANIN lesions were also present in the pancreatic cancer sections. These lesions displayed weak MUC16 staining. Samples collected at surgical resection showed MUC16 positive cytoplasmic staining in the stromal fibroblasts, and apical cytoplasmic staining in the tumor (Figure 1D). These results indicate that MUC16 is a feasible target for FGS in the key patient population of interest.

Synthesis and *In vitro* validation of MUC16 Expression

To develop a targeted FGS probe, AR9.6 and isotype-specific IgG control antibody were conjugated to the NIR dye, IRDye800 NHS Ester. AR9.6-IRDye800 and IgG-IRDye800 antibody conjugates were synthesized by reacting NHS ester dye with free amines on the antibody to form stable amide bonds (Figure 2A). IgG was used as a non-specific isotype control throughout this study. Conjugation reactions resulted in an average of 3 dyes per protein as determined by absorbance spectroscopy (Figure 2B). Fluorescence spectra of the antibody conjugates demonstrated that fluorescence was not quenched upon conjugation to the protein.

The expression of MUC16 was assessed by western blot in 5 pancreatic cancer cell lines: T3M4, Capan1, Colo357, CFPAC, and HPAC (Figure 2C). An immortalized normal pancreas cell line (HPNE) served as a negative control, and the ovarian cancer cell line,

OVCAR3, which has well-documented MUC16 expression, served as a positive control (25,26). A range of moderate to high expression of MUC16 was seen across all pancreatic cancer cell lines. To confirm that conjugation of AR9.6 to IRDye800 did not drastically impact antigen recognition and cell binding, a fluorescent western blot and fluorescence microscopy were conducted, as shown in Figure 2D and 2E. Fluorescent western blotting in the 800 nm channel demonstrated that AR9.6-IRDye800 could still recognize MUC16 after dye conjugation. Secondary antibody binding (700 nm channel) confirmed that the fluorescence seen in the 800 nm channel was due to the presence of AR9.6-IRDye800 binding, as shown by colocalization between the 700 and 800 nm channels in Figure 2D. As expected, the non-specific IgG-IRDye800 conjugate did not bind to MUC16, and secondary antibody staining confirmed that AR9.6 was not present. Fluorescence microscopy showed strong fluorescence signal from AR9.6-IRDye800 in MUC16 expressing pancreatic cancer cell lines, which was consistent with OVCAR3 cells (positive control). AR9.6-IRDye800 did not bind to MUC16 negative HPNE cells, and the IgG-IRDye800 control did not bind to cells, regardless of MUC16 expression levels (Figure 2E).

Determination of AR9.6-IRDye800 optimal imaging time from tumor signal dynamics

To monitor the tumor accumulation of the antibody conjugates over time, AR9.6-IRDye800, IgG-IRDye800, and unconjugated IRDye800 were assessed for 6 days in a subcutaneous T3M4 xenograft model of pancreatic cancer. Figure 3A depicts representative images of tumor accumulation from the three groups over 144 h based on images acquired daily on the Pearl® Trilogy. Strong fluorescence signal was observed throughout the mouse at 4 h, while robust enhancement of the tumor was observed within 24 h after injection of AR9.6-IRDye800, and signal was retained in the tumor at 144 h. Diffuse signal was observed with IgG-IRDye800 at 24 h, while unconjugated IRDye800 was cleared within 24 h as expected (27). Tumor to background ratios (TBRs) were highest for AR9.6-IRDye800 at 144 h after injection (4.47 ± 1.43), as compared to 2.12 ± 0.12 for the IgG-IRDye800 control and 0.89 ± 0.11 for the unconjugated IRDye800 (Figure 3B). The TBR for AR9.6-IRDye800 was significantly higher ($p < 0.0001$) than IgG-IRDye800 at 144 h (the peak TBR for the IgG control). Signal to noise ratios (SNRs) were also calculated for the three groups (Figure 3B). At 144 h, AR9.6-IRDye800 still showed significantly higher ($p = 0.0492$) SNR (94.35 ± 33.66) than IgG-IRDye800 (48.18 ± 6.68) and IRDye800 (5.56 ± 1.24). Tumor accumulation of AR9.6-IRDye800 in Colo357 xenografts (Supplemental Figure 1) resulted in comparable TBR (N=4, TBR =5.63 ± 0.70) to the T3M4 xenografts. The function of both the TBR and SNR metrics for imaging has been previously reviewed (28). *In vitro* analysis of the cellular kinetics of AR9.6-IRDye800 binding shown in Supplemental Figure 3 suggests that antibody internalization, and lysosomal degradation, may contribute in part to the decrease in fluorescence signal over time (29).

To further assess the specificity of the AR9.6 conjugate for the tumor, all T3M4 xenograft tumors and clearance organs were collected at 144 h post-injection and imaged on the Pearl® Trilogy to analyze fluorescence signal in key clearance organs as shown in Supplemental Figure 2. Quantification of tumor signal demonstrated a significant 2.18-fold increase in mean fluorescence intensity in the AR9.6-IRDye800 tumors compared to the IgG-IRDye800 ($p<0.0001$). AR9.6-IRDye800 also showed significantly lower signal in the

liver at the 144 h time point when compared to the IgG control (p= 0.0120). AR9.6-IRDye800 displayed a 2.65-fold increase in tumor signal compared to AR9.6-IRDye800 liver signal (p<0.0001). Conversely, the IgG-IRDye800 control showed higher liver signal than tumor signal. These results demonstrate the specificity and retention of the AR9.6 conjugate for tumor detection. Additionally, higher fluorescent signal was observed in the tumor compared to the liver, suggesting that AR9.6-IRDye800 could potentially highlight metastatic lesions on key background tissues in future studies.

Fluorescence-Guided Surgery

FGS of orthotopic pancreatic cancer xenografts was conducted on multiple FGS systems, as depicted in Figure 4. The FDA-approved Fluobeam 800 imaging system provided real-time intraoperative feedback via a single 800 nm channel display system (12). Using Fluobeam 800 guidance, AR9.6-IRDye800 provided robust tumor enhancement against background organs, including the liver (Figure 4A). Conversely, there was variable and negligible fluorescence in the IgG-IRDye800 group, and the signal in the liver was brighter than tumor signal (Figure 4B). As shown in Figure 4C, the mean intraoperative TBR for AR9.6-IRDye800 (3.75 ± 0.29) was significantly higher than the mean intraoperative TBR for IgG-IRDye800 (1.89 ± 0.55) (p = 0.0010). Videos of AR9.6-IRDye800 and IgG-IRDye800 tumor enhancement during resection can be viewed in Supplemental Videos 1 and 2. The Lab Flare RP1 image-guided surgery system (currently restricted to preclinical studies) was used to confirm AR9.6-IRDye800 signal with real-time NIR-color channel display. Images on this system also showed strong contrast-enhancement with AR9.6-IRDye800. Tumor was clearly delineated against healthy pancreas, and additional lesions could be seen on the posterior surface of the pancreas (Figure 4D).

Biodistribution of fluorescent antibody conjugates was analyzed in necropsied organs after FGS (Figure 5A). Quantification of the biodistribution demonstrated significantly higher mean fluorescent signal in the tumors with AR9.6-IRDye800 (0.05 ± 0.006) compared to the IgG-IRDye800 control (0.014 ± 0.009) (p = 0.0009) (Figure 5B). There were no significant differences in mean signal between any of the other organs. Variable fluorescent signal was observed in the stomach due to autofluorescence from the mouse diet. Signal in the liver and kidneys can be attributed to clearance of the antibody-dye conjugate and released dye, respectively. The mean tumor SNRs of AR9.6-IRDye800 (94.09 ±11.95) and IgG-IRDye800 (28.33 ± 18.67) were also significantly different (p = 0.0010).

Necropsied organs were also analyzed with a spectrophotometric device. Spectra were collected at defined points across the tumor. Figure 6A and 6B depict the integrated fluorescence emission spectra that correspond to each point excitation. Fluorescent enhancement of the tumor tissue corresponded to an increase in area under the curve from spectral acquisition. Furthermore, colocalization between fluorescent signal and the presence of tumor tissue can be seen in H&E staining. Resected specimens were confirmed as poorly-differentiated tumors by a board-certified pathologist. AR9.6-IRDye800 showed increased signal from fluorescence images as well as wavelength resolved measurements compared to the IgG-IRDye800 control. Tumor sections embedded in OCT were analyzed for the presence of AR9.6-IRDye800 and IgG-IRDye800 (Figure 6C). NIR fluorescence was

detected in tumors from mice that were administered AR9.6-IRDye800, while NIR fluorescence was not detected in tumor sections from mice administered IgG-IRDye800.

As shown in Figure 7, micro-metastatic lesions were identified during AR9.6-IRDye800-guided resection. NIR signal was readily detected in spleen, muscle, and lung metastases. H&E staining of resected OCT embedded specimens demonstrated the presence of tumor tissue in the detected metastatic lesions. Metastatic lesions were confirmed by a board-certified pathologist (G.A.T). Fluorescence microscopy demonstrated the presence of AR9.6-IRDye800 in the tumor tissue. Fluorescent signal from AR9.6-IRDye800 was consistent with the location of the metastatic lesions, whereas adjacent resected tissue had no visible fluorescence present. Fluorescence localization in the metastatic lesions demonstrated high specificity of AR9.6-IRDye800 for the tumor tissue.

DISCUSSION

MUC16 is widely expressed in the tumors of patients with pancreatic, ovarian, gastric, esophageal, and colon cancer, among others (18). Since MUC16 is natively expressed in normal bronchial, ovarian, endometrial, and corneal cells in the body, there is high potential for low background signal from key organs during pancreatic cancer imaging (19). Furthermore, in comparison to other targets in pancreatic cancer such as CEA and CA-19–9, MUC16 can better differentiate between chronic pancreatitis and pancreatic cancer (21). Thus, there is compelling evidence to support the development of MUC16 as a target for image-guided surgical intervention of pancreatic cancer.

Compared to current FGS probes in clinical trials, AR9.6-IRDye800 has several potential advantages. EGFR, the target of cetuximab-IRDye800 and panitumumab-IRDye800, has variable expression levels across pancreatic cancer (30). EGFR is also expressed in the healthy pancreas, chronic pancreatitis, and normal stomach and duodenal tissues, which could contribute to elevated background signal during intraoperative pancreatic cancer imaging (16,31). In comparison, MUC16 is highly expressed in pancreatic cancer tissues, is not expressed in the normal pancreas, and is not expressed in key background tissues, which could improve contrast with FGS. However, results from the Phase I/II cetuximab-IRDye800 trial showed promising results for using EGFR as a target for imaging (NCT02736578). One of the major strengths of this study was the use of multimodal imaging in combining FGS with photoacoustic imaging to improve the depth of penetration. EGFR is also advantageous in that it is present in a wide variety of malignancies, and can be used as a tumor-agnostic FGS target. Additionally, SGM-101 is another antibody-targeted probe that has demonstrated success in a Phase I clinical trial by targeting the tumor antigen CEA (NCT02973672). However, the use of a 700 nm NIR dye limited the depth of penetration of FGS and introduced problems with autofluorescence. Results have not been reported, to date, from the panitumumab-IRDye800, or bevacizumab-IRDye800 (PENGUIN) studies (NCT03384238, NCT02743975). While MUC16 is relatively unexplored as an imaging target in comparison to EGFR and CEA, there is similar potential to utilize this probe to guide resection of a variety of solid tumors.

AR9.6-IRDye800 demonstrates comparable or improved tumor delineation in comparison to other preclinical studies. Preclinical studies conducted with panitumumab-IRDye800 (now in a Phase I/II trial for pancreatic cancer) in a subcutaneous model of head and neck cancer showed TBRs of 2.9 using an IRDye800 optimized system. Comparatively, with AR9.6-IRDye800 in a subcutaneous pancreatic cancer model, an IRDye800 optimized imaging system yielded a TBR of 4.7 and 5.6 across two different cell types. Both AR9.6-IRDye800 and panitumumab IRDye800 had significantly higher tumor signal using the targeted agent as compared to an IgG control (32). In an orthotopic model, panitumumab-IRDye800 had a mean intraoperative TBR of 4.2 compared to a mean intraoperative TBR of 3.75 with AR9.6-IRDye800in the orthotopic model. Preclinical studies with SGM-101 (completed Phase 1 clinical trial), performed similarly to AR9.6-IRDye800 with intraoperative TBRs to of 3.5 in an orthotopic pancreatic cancer model. Preclinical studies with a humanized CEA antibody (hM5A) conjugated to IRDye800 also showed a mean TBR of 3.5 in a patient-derived orthotopic xenograft model (33). Similar results have also been shown in studies using targeting agents other than antibody conjugates in preclinical pancreatic cancer FGS studies. An αvβ6 integrin targeting peptide yielded TBRs of 2.7 intraoperatively in an orthotopic model (34). An antibody fragment, ssSM3E/800CW, targeting CEA, displayed a mean TBRs of 2.37 in an orthotopic model of pancreatic cancer (35). TBRs achieved under AR9.6-IRDye800 guidance in this study met the recommended TBR of >3.0 for preclinical studies, suggesting that this probe is a potential candidate for clinical translation (28).

Pancreatic cancer surgeries are complex and often result in recurrence. Despite the challenges of targeting this aggressive tumor model, there is an unmet clinical need to improve surgical outcomes. Due to the heterogeneity of pancreatic tumors, initial clinical trials with existing targeted probes have seen only modest tumor enhancement under FGS (17). Future clinical trials in pancreatic cancer will likely incorporate a panel of FGS probes to more accurately capture the tumor heterogeneity and improve intraoperative contrast and enhancement for improved resections (36). However, the feasibility of incorporating multiple probes needs to be investigated to determine if multiple targets improve overall contrast. Because of the well-documented role of mucins in pancreatic cancer, AR9.6-IRDye800 has strong potential to improve current FGS in pancreatic cancer. Thus, we have identified an additional target for FGS that is widely expressed in pancreatic cancer patients.

Identification of occult peritoneal metastases is critical in FGS. Pre-operative imaging modalities can accurately predict unresectability in pancreatic cancer but fall short in detecting small metastatic lesions, identifying vascular involvement, and differentiating benign conditions (37). Thus, FGS can be beneficial in identifying metastases that may have been missed on initial imaging scans. This will impact the course of treatment for pancreatic cancer patients, as the presence of metastatic lesions determines the resectability of the tumor (38). In this study, AR9.6-IRDye800 identified multiple metastatic lesions in the muscle, lung, and spleen. This suggests that AR9.6-IRDye800-guided resection could potentially improve the identification of missed lesions during surgery. Further studies are needed to investigate the detection capabilities of micro-metastases in patient samples.

This study demonstrates the feasibility and proof-of-concept for MUC16 as a potential target and warrants further investigation. The AR9.6 antibody used here was a murine antibody

that can recognize both mouse and human MUC16 and is thus limited in its translational potential, because of potentially high levels of immunogenicity. However, this antibody was chosen for investigation because a humanized AR9.6 antibody is under development, and future studies will investigate the humanized antibody for clinical translation. Additionally, because of variations in tumor size, not all of the orthotopic xenografts had sufficient unaffected healthy pancreas remaining at the time of FGS. Thus, TBR was calculated using either remaining adjacent normal pancreas or adjacent peritoneal tissue as background signal. Future studies will standardize tumor size and calculate TBR in the adjacent healthy pancreas or inflammatory tissue. Additionally, the optimal dye: protein ratio for AR9.6-IRDye800 imaging of pancreatic cancer, as well as methods for site-specific conjugation, will also be investigated. Furthermore, this study does not address the role of tumor heterogeneity on intraoperative fluorescence contrast. Since dense stroma and heterogeneous cell populations can impact the deposition of antibody probes as well as drugs, particularly in pancreatic cancer, further studies are needed to explore FGS in the context of varying cell populations. Discrepancies between experimental studies and clinical results in pancreatic cancer can be attributed in part to inaccurate or ineffective recapitulation of the tumor stroma and microenvironment (39). Genetically engineered mouse models or patient-derived xenograft models must be employed to more accurately depict the complexity of both the tumor and stroma in pancreatic cancer, though these models have limitations as well. The presence of dense stroma may also impede the delivery of antibodies, and smaller antibody fragments should be investigated to optimize tumor penetration and intratumoral distribution (40–42).

Additionally, the identification of metastatic lymph nodes during surgery is a key component of treating pancreatic cancer patients (43). Lymph node status is an important predictor of survival, and identification of regional lymph node involvement (N1 disease) may influence the course of adjuvant therapy (44). Thus, robust identification of N1 disease and the extent of node involvement with FGS could be beneficial in determining treatment, and sufficient nodal resection. This study did not specifically investigate the presence of MUC16 in metastatic lymph nodes. Future studies are needed to explore the prevalence of MUC16 in positive lymph nodes, and the potential for AR9.6-IRDye800 to identify positive lymph nodes during surgery. Finally, the ectodomain of MUC16 can be cleaved and has been found to circulate in the bloodstream in several cancers, which could impact the feasibility of MUC16 as a target in cancer. Cleavage and subsequent circulation of the antigen may impact the amount of the antibody that actually reaches the tumor. However, a large body of work has demonstrated feasibility for targeting and imaging various cleaved antigens (45–48).

Herein, we developed a MUC16-targeted NIR fluorescent antibody probe and demonstrated its efficacy in delineating pancreatic cancer intraoperatively *in vitro* and *in vivo* by fluorescence-guided surgery. AR9.6-IRDye800 imaging resulted in significantly higher tumor signal compared to an IgG-IRDye800 control. Enhanced tumors could be distinguished from healthy tissue and key background organs relevant to pancreatic cancer. AR9.6-IRDye800 guidance also enabled the detection of micro-metastatic lesions in an orthotopic xenograft tumor model. This data suggests that AR9.6-IRDye800 has the potential for clinical translation as a probe for surgical resection of pancreatic cancer.

Supplementary Material

Refer to Web version on PubMed Central for supplementary material.

ACKNOWLEDGEMENTS

The authors thank Dr. Denis Svechkarev for his assistance with optical probe development, Dr. Madi Madiyalakan (OncoQuest, Inc.; Edmonton, Alberta, Canada) for his assistance with antibody acquisition, AJ Crawford for her assistance with orthotopic surgical techniques, and Constance McKee (Manzanita Pharmaceuticals, Inc.; Woodside, CA, USA) for providing the Fluobeam imaging system. This work was supported by NIH grants, U01CA210240 (TAH), P30CA036727 (Fred and Pamela Buffett Cancer Center at UNMC), CA208108 (PR), T32CA009476 (MTO) and the Nebraska Research Initiative (AMM).

ABBREVIATIONS

FGS	fluorescence-guided surgery
PDAC	pancreatic ductal adenocarcinoma
NIR	near-infrared
EGFR	epidermal growth factor receptor
VEGF	vascular endothelial growth factor
CEA	carcinoembryonic antigen
mAb	monoclonal antibody
ROI	region of interest
TBR	tumor to background ratio
SNR	signal to noise ratio
OCT	optimal cutting temperature compound
H&E	Hematoxylin and Eosin
UNMC	University of Nebraska Medical Center

REFERENCES

1. McGuigan A, Kelly P, Turkington RC, Jones C, Coleman HG, McCain RS. Pancreatic cancer: A review of clinical diagnosis, epidemiology, treatment and outcomes. World J Gastroenterol [Internet]. Baishideng Publishing Group Inc; 2018 [cited 2019 Dec 2];24:4846–61. Available from: http://www.ncbi.nlm.nih.gov/pubmed/30487695
2. Tempero MA, Malafa MP, Al-Hawary M, Asbun H, Bain A, Behrman SW, et al. Pancreatic adenocarcinoma, version 2.2017: Clinical practice guidelines in Oncology. JNCCN J. Natl. Compr. Cancer Netw. Harborside Press; 2017. page 1028–61.
3. Merkow RP, Bilimoria KY, Bentrem DJ, Pitt HA, Winchester DP, Posner MC, et al. National Assessment of Margin Status as a Quality Indicator after Pancreatic Cancer Surgery. Ann Surg Oncol [Internet]. Springer US; 2014 [cited 2018 Dec 18];21:1067–74. Available from: 10.1245/s10434-013-3338-2

4. Barugola G, Partelli S, Marcucci S, Sartori N, Capelli P, Bassi C, et al. Resectable Pancreatic Cancer: Who Really Benefits From Resection? Ann Surg Oncol [Internet]. Springer-Verlag; 2009 [cited 2018 Sep 11];16:3316–22. Available from: 10.1245/s10434-009-0670-7
5. Niesen W, Hank T, Büchler M, Strobel O. Local radicality and survival outcome of pancreatic cancer surgery. Ann Gastroenterol Surg [Internet]. Wiley-Blackwell; 2019 [cited 2019 Oct 9];3:464–75. Available from: http://www.ncbi.nlm.nih.gov/pubmed/31549006
6. Konstantinidis IT, Warshaw AL, Allen JN, Blaszkowsky LS, Castillo CF, Deshpande V, et al. Pancreatic Ductal Adenocarcinoma. Ann Surg [Internet]. 2013 [cited 2019 Nov 21];257:731–6. Available from: http://www.ncbi.nlm.nih.gov/pubmed/22968073
7. Frangioni JV. New technologies for human cancer imaging. J. Clin. Oncol. 2008. page 4012–21. [PubMed: 18711192]
8. Zhang RR, Schroeder AB, Grudzinski JJ, Rosenthal EL, Warram JM, Pinchuk AN, et al. Beyond the margins: real-time detection of cancer using targeted fluorophores. Nat Rev Clin Oncol [Internet]. Nature Publishing Group, a division of Macmillan Publishers Limited. All Rights Reserved.; 2017;14:347–64. Available from: 10.1038/nrclinonc.2016.212
9. Lwin TM, Hoffman RM, Bouvet M. The development of fluorescence guided surgery for pancreatic cancer: from bench to clinic. Expert Rev Anticancer Ther [Internet]. 2018 [cited 2019 Jul 1];18:651–62. Available from: 10.1080/14737140.2018.1477593
10. Pansare VJ, Hejazi S, Faenza WJ, Prud'homme RK. Review of Long-Wavelength Optical and NIR Imaging Materials: Contrast Agents, Fluorophores, and Multifunctional Nano Carriers. Chem Mater [Internet]. American Chemical Society; 2012;24:812–27. Available from: 10.1021/cm2028367
11. Hong G, Antaris AL, Dai H. Near-infrared fluorophores for biomedical imaging. Nat Biomed Eng [Internet]. Nature Publishing Group; 2017 [cited 2017 Nov 13];1:0010. Available from: http://www.nature.com/articles/s41551-016-0010
12. DSouza A V, Lin H, Henderson ER, Samkoe KS, Pogue BW. Review of fluorescence guided surgery systems: identification of key performance capabilities beyond indocyanine green imaging. J Biomed Opt [Internet]. Society of Photo-Optical Instrumentation Engineers; 2016 [cited 2017 Nov 20];21:080901. Available from: http://www.ncbi.nlm.nih.gov/pubmed/27533438
13. Olson MT, Ly QP, Mohs AM. Fluorescence Guidance in Surgical Oncology: Challenges, Opportunities, and Translation. Mol Imaging Biol [Internet]. Springer International Publishing; 2019 [cited 2019 Nov 22];21:200–18. Available from: 10.1007/s11307-018-1239-2
14. Kobayashi H, Choyke PL, Ogawa M. Monoclonal antibody-based optical molecular imaging probes; considerations and caveats in chemistry, biology and pharmacology. Curr Opin Chem Biol [Internet]. Elsevier Current Trends; 2016 [cited 2017 Oct 18];33:32–8. Available from: http://www.sciencedirect.com/science/article/pii/S1367593116300540
15. Wittrup KD, Thurber GM, Schmidt MM, Rhoden JJ. Practical Theoretic Guidance for the Design of Tumor-Targeting Agents. Methods Enzymol [Internet]. Academic Press; 2012 [cited 2019 Nov 21]. page 255–68. Available from: https://www.sciencedirect.com/science/article/pii/B9780123969620000100?via%3Dihub
16. Tummers WS, Miller SE, Teraphongphom NT, Gomez A, Steinberg I, Huland DM, et al. Intraoperative Pancreatic Cancer Detection using Tumor-Specific Multimodality Molecular Imaging. Ann Surg Oncol [Internet]. NIH Public Access; 2018 [cited 2019 Jun 26];25:1880–8. Available from: http://www.ncbi.nlm.nih.gov/pubmed/29667116
17. Hoogstins CES, Boogerd LSF, Sibinga Mulder BG, Mieog JSD, Swijnenburg RJ, van de Velde CJH, et al. Image-Guided Surgery in Patients with Pancreatic Cancer: First Results of a Clinical Trial Using SGM-101, a Novel Carcinoembryonic Antigen-Targeting, Near-Infrared Fluorescent Agent. Ann Surg Oncol [Internet]. Springer; 2018 [cited 2018 Dec 10];25:3350–7. Available from: http://www.ncbi.nlm.nih.gov/pubmed/30051369
18. Streppel MM, Vincent A, Mukherjee R, Campbell NR, Chen S-H, Konstantopoulos K, et al. Mucin 16 (cancer antigen 125) expression in human tissues and cell lines and correlation with clinical outcome in adenocarcinomas of the pancreas, esophagus, stomach, and colon. Hum Pathol [Internet]. NIH Public Access; 2012 [cited 2018 Jun 5];43:1755–63. Available from: http://www.ncbi.nlm.nih.gov/pubmed/22542127

19. Felder M, Kapur A, Gonzalez-Bosquet J, Horibata S, Heintz J, Albrecht R, et al. MUC16 (CA125): tumor biomarker to cancer therapy, a work in progress. Mol Cancer [Internet]. BioMed Central; 2014 [cited 2019 Nov 21];13:129. Available from: http://www.ncbi.nlm.nih.gov/pubmed/24886523
20. Haridas D, Chakraborty S, Ponnusamy MP, Lakshmanan I, Rachagani S, Cruz E, et al. Pathobiological Implications of MUC16 Expression in Cancer Pancreatic. Srivastava RK, editor. PLoS One [Internet]. Public Library of Science; 2011 [cited 2018 Feb 9];6:e26839. Available from: 10.1371/journal.pone.0026839
21. Jiang K, Tan E, Sayegh Z, Centeno B, Malafa M, Coppola D. Cancer Antigen 125 (CA125, MUC16) Protein Expression in the Diagnosis and Progression of Pancreatic Ductal Adenocarcinoma. Appl Immunohistochem Mol Morphol [Internet]. 2017 [cited 2018 Sep 24];25:620–3. Available from: http://insights.ovid.com/crossref?an=00129039-201710000-00004
22. Qi B, Crawford AJ, Wojtynek NE, Holmes MB, Souchek JJ, Almeida-Porada G, et al. Indocyanine green loaded hyaluronan-derived nanoparticles for fluorescence-enhanced surgical imaging of pancreatic cancer. Nanomedicine Nanotechnology, Biol Med [Internet]. 2018 [cited 2018 Dec 10];14:769–80. Available from: 10.1016/j.nano.2017.12.015
23. Hill TK, Kelkar SS, Wojtynek NE, Souchek JJ, Payne WM, Stumpf K, et al. Near Infrared Fluorescent Nanoparticles Derived from Hyaluronic Acid Improve Tumor Contrast for Image-Guided Surgery. Theranostics [Internet]. Ivyspring International Publisher; 2016 [cited 2017 Nov 14];6:2314–28. Available from: http://www.ncbi.nlm.nih.gov/pubmed/27877237
24. Mohs AM, Mancini MC, Singhal S, Provenzale JM, Leyland-Jones B, Wang MD, et al. Hand-held spectroscopic device for in vivo and intraoperative tumor detection: contrast enhancement, detection sensitivity, and tissue penetration. Anal Chem. 2010;82:9058–65. [PubMed: 20925393]
25. Thériault C, Pinard M, Comamala M, Migneault M, Beaudin J, Matte I, et al. MUC16 (CA125) regulates epithelial ovarian cancer cell growth, tumorigenesis and metastasis. Gynecol Oncol [Internet]. Academic Press; 2011 [cited 2018 Mar 12];121:434–43. Available from: https://www.sciencedirect.com/science/article/pii/S0090825811001405?via%3Dihub
26. Gao Y, Hernandez C, Yuan H-X, Lilly J, Kota P, Zhou H, et al. Ultrasound molecular imaging of ovarian cancer with CA-125 targeted nanobubble contrast agents. Nanomedicine Nanotechnology, Biol Med [Internet]. Elsevier; 2017 [cited 2019 Jul 3];13:2159–68. Available from: https://www.sciencedirect.com/science/article/pii/S1549963417301077?via%3Dihub
27. Marshall M V, Draney D, Sevick-Muraca EM, Olive DM. Single-dose intravenous toxicity study of IRDye 800CW in Sprague-Dawley rats. Mol Imaging Biol [Internet]. Springer; 2010 [cited 2018 Jan 4];12:583–94. Available from: http://www.ncbi.nlm.nih.gov/pubmed/20376568
28. Tummers WS, Warram JM, van den Berg NS, Miller SE, Swijnenburg RJ, Vahrmeijer AL, et al. Recommendations for reporting on emerging optical imaging agents to promote clinical approval. Theranostics. Ivyspring International Publisher; 2018. page 5336–47.
29. Cilliers C, Liao J, Atangcho L, Thurber GM. Residualization Rates of Near-Infrared Dyes for the Rational Design of Molecular Imaging Agents. Mol Imaging Biol. Springer New York LLC; 2015;17:757–62. [PubMed: 25869081]
30. Oliveira-Cunha M, Newman WG, Siriwardena AK. Epidermal Growth Factor Receptor in Pancreatic Cancer. Cancers (Basel) [Internet]. 2011 [cited 2019 Dec 3];3:1513–26. Available from: http://www.mdpi.com/2072-6694/3/2/1513
31. Tummers WS, Farina-Sarasqueta A, Boonstra MC, Prevoo HA, Sier CF, Mieog JS, et al. Selection of optimal molecular targets for tumor-specific imaging in pancreatic ductal adenocarcinoma. Oncotarget [Internet]. Impact Journals; 2017 [cited 2019 Nov 25];8:56816–28. Available from: http://www.oncotarget.com/fulltext/18232
32. Heath CH, Deep NL, Sweeny L, Zinn KR, Rosenthal EL. Use of Panitumumab-IRDye800 to Image Microscopic Head and Neck Cancer in an Orthotopic Surgical Model. Ann Surg Oncol [Internet]. Springer-Verlag; 2012 [cited 2019 Apr 30];19:3879–87. Available from: 10.1245/s10434-012-2435-y
33. Lwin TM, Miyake K, Murakami T, DeLong JC, Amirfakhri S, Filemoni F, et al. Fluorescent humanized anti-CEA antibody specifically labels metastatic pancreatic cancer in a patient-derived orthotopic xenograft (PDOX) mouse model. Oncotarget. Impact Journals LLC; 2018;9:37333–42.

34. Tummers WS, Kimura RH, Abou-Elkacem L, Beinat C, Vahrmeijer AL, Swijnenburg R-J, et al. Development and Preclinical Validation of a Cysteine Knottin Peptide Targeting Integrin αvβ6 for Near-infrared Fluorescent-guided Surgery in Pancreatic Cancer. Clin Cancer Res [Internet]. American Association for Cancer Research; 2018 [cited 2018 Mar 13];24:1667–76. Available from: http://www.ncbi.nlm.nih.gov/pubmed/29298796
35. Boonstra MC, Tolner B, Schaafsma BE, Boogerd LSF, Prevoo HAJ, Bhavsar G, et al. Preclinical evaluation of a novel CEA-targeting near-infrared fluorescent tracer delineating colorectal and pancreatic tumors. Int J Cancer [Internet]. NIH Public Access; 2015 [cited 2018 Jul 5];137:1910–20. Available from: http://www.ncbi.nlm.nih.gov/pubmed/25895046
36. Vahrmeijer AL, Hutteman M, van der Vorst JR, van de Velde CJH, Frangioni JV. Image-guided cancer surgery using near-infrared fluorescence. Nat Rev Clin Oncol [Internet]. NIH Public Access; 2013 [cited 2017 Nov 20];10:507–18. Available from: http://www.ncbi.nlm.nih.gov/pubmed/23881033
37. Zhang L, Sanagapalli S, Stoita A. Challenges in diagnosis of pancreatic cancer. World J Gastroenterol. Baishideng Publishing Group Inc.; 2018;24:2047–60. [PubMed: 29785074]
38. Liu X, Fu Y, Chen Q, Wu J, Gao W, Jiang K, et al. Predictors of distant metastasis on exploration in patients with potentially resectable pancreatic cancer. BMC Gastroenterol [Internet]. 2018 [cited 2020 Jan 13];18:168. Available from: https://bmcgastroenterol.biomedcentral.com/articles/10.1186/s12876-018-0891-y [PubMed: 30400836]
39. Erkan M, Hausmann S, Michalski CW, Fingerle AA, Dobritz M, Kleeff J, et al. The role of stroma in pancreatic cancer: diagnostic and therapeutic implications. Nat Rev Gastroenterol Hepatol [Internet]. Nature Publishing Group; 2012 [cited 2020 Feb 27];9:454–67. Available from: http://www.nature.com/articles/nrgastro.2012.115
40. Dougan M, Ingram JR, Jeong HJ, Mosaheb MM, Bruck PT, Ali L, et al. Targeting cytokine therapy to the pancreatic tumor microenvironment using PD-L1–specific VHHs. Cancer Immunol Res. American Association for Cancer Research Inc.; 2018;6:389–401. [PubMed: 29459478]
41. Xenaki KT, Oliveira S, van Bergen En Henegouwen PMP. Antibody or Antibody Fragments: Implications for Molecular Imaging and Targeted Therapy of Solid Tumors. Front Immunol [Internet]. Frontiers Media SA; 2017 [cited 2018 Aug 14];8:1287. Available from: http://www.ncbi.nlm.nih.gov/pubmed/29075266
42. Rochefort MM, Girgis MD, Knowles SM, Ankeny JS, Salazar F, Wu AM, et al. A Mutated Anti-CA19–9 scFv-Fc for Positron Emission Tomography of Human Pancreatic Cancer Xenografts. Mol Imaging Biol. Springer New York LLC; 2014;16:721–9. [PubMed: 24691872]
43. Eskander MF, de Geus SWL, Kasumova GG, Ng SC, Al-Refaie W, Ayata G, et al. Evolution and impact of lymph node dissection during pancreaticoduodenectomy for pancreatic cancer. Surgery [Internet]. Mosby; 2017 [cited 2019 Nov 21];161:968–76. Available from: https://www.sciencedirect.com/science/article/pii/S0039606016306183?via%3Dihub
44. Ashfaq A, Pockaj BA, Gray RJ, Halfdanarson TR, Wasif N. Nodal Counts and Lymph Node Ratio Impact Survival After Distal Pancreatectomy for Pancreatic Adenocarcinoma. J Gastrointest Surg [Internet]. Springer US; 2014 [cited 2019 Nov 21];18:1929–35. Available from: 10.1007/s11605-014-2566-5
45. Ulmert D, Evans MJ, Holland JP, Rice SL, Wongvipat J, Pettersson K, et al. Imaging Androgen Receptor Signaling with a Radiotracer Targeting Free Prostate-Specific Antigen. Cancer Discov [Internet]. American Association for Cancer Research; 2012 [cited 2019 Nov 19];2:320–7. Available from: http://www.ncbi.nlm.nih.gov/pubmed/22576209
46. Sharma SK, Sevak KK, Monette S, Carlin SD, Knight JC, Wuest FR, et al. Preclinical (89)Zr Immuno-PET of High-Grade Serous Ovarian Cancer and Lymph Node Metastasis. J Nucl Med [Internet]. 2016;57:771–6. Available from: http://www.ncbi.nlm.nih.gov/pmc/articles/PMC4959443/
47. Viola-Villegas NT, Rice SL, Carlin S, Wu X, Evans MJ, Sevak KK, et al. Applying PET to Broaden the Diagnostic Utility of the Clinically Validated CA19.9 Serum Biomarker for Oncology. J Nucl Med [Internet]. NIH Public Access; 2013 [cited 2019 Nov 19];54:1876–82. Available from: http://www.ncbi.nlm.nih.gov/pubmed/24029655
48. Liu JF, Moore KN, Birrer MJ, Berlin S, Matulonis UA, Infante JR, et al. Phase I study of safety and pharmacokinetics of the anti-MUC16 antibody–drug conjugate DMUC5754A in patients with

platinum-resistant ovarian cancer or unresectable pancreatic cancer. Ann Oncol [Internet]. 2016 [cited 2020 Feb 24];27:2124–30. Available from: https://reader.elsevier.com/reader/sd/pii/S0923753419358417?token=74E24D7749FC78D2402357A631429B6A1486A720A291EBE21CA15CDE26DEB08CAAB73CDE5B514F1D88592F7503E93BEA

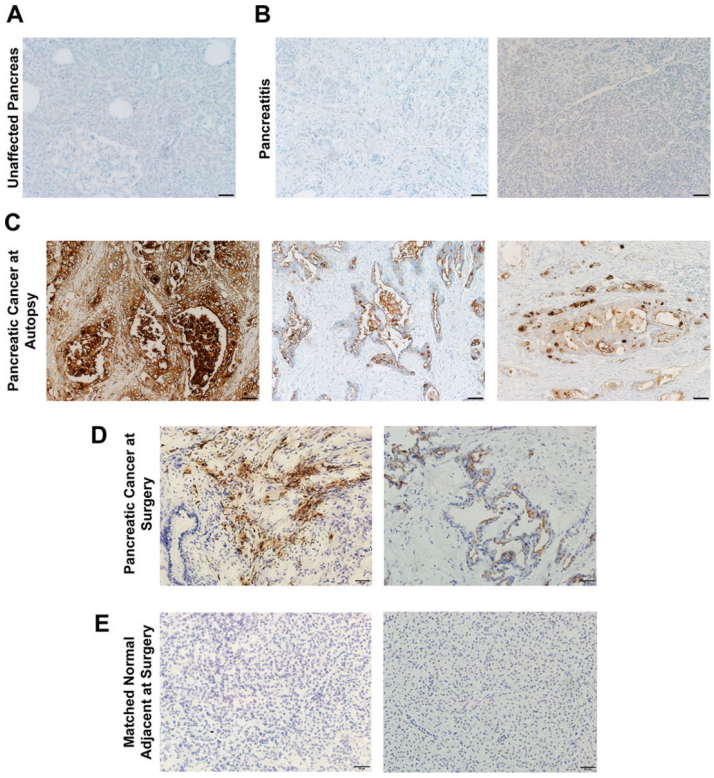

Figure 1.

MUC16 expression in human pancreatic ductal adenocarcinoma samples. (A) Unaffected pancreas (B) pancreatitis (C) pancreatic cancer samples collected at autopsy. (D) Pancreatic cancer resected at the time of surgery and (E) matched normal adjacent tissue collected at the time of surgery. All images acquired at 200X magnification. Scale bar = 50 μm.

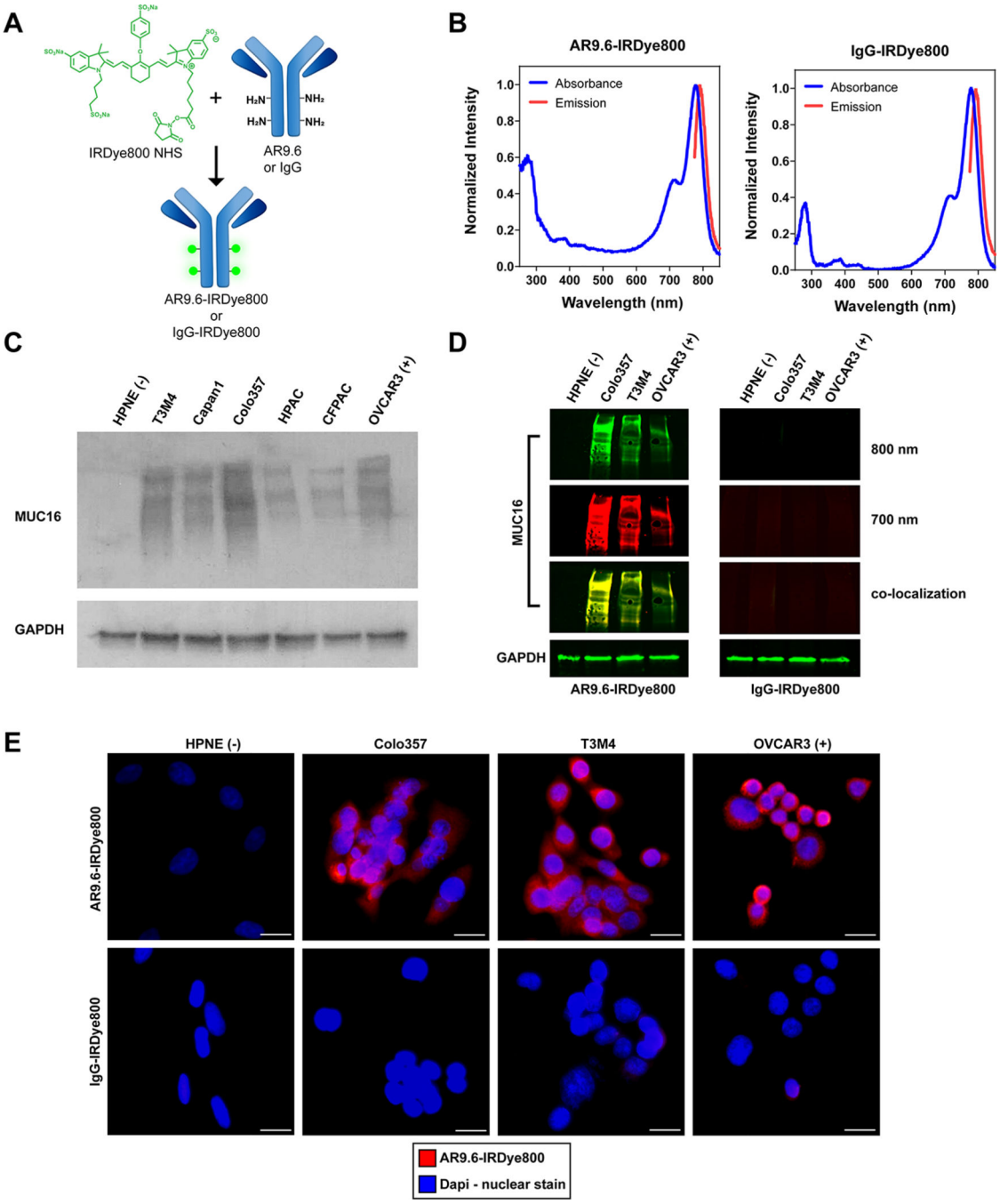

Figure 2.

Synthesis and *in vitro* characterization of antibody conjugates. (A) Schematic of IRDye800 NHS Ester conjugation to AR9.6 and IgG. (B) Representative absorbance and emission spectra from both antibody conjugates. (C) Western blot of MUC16 expression in human pancreatic cancer cell lines. (D) Fluorescent western blot confirming binding of AR9.6-IRDye800, and lack of binding in IgG control. (E) Immunofluorescence of antibody conjugate binding. Images acquired at 400X magnification. Scale bar = 20 μm.

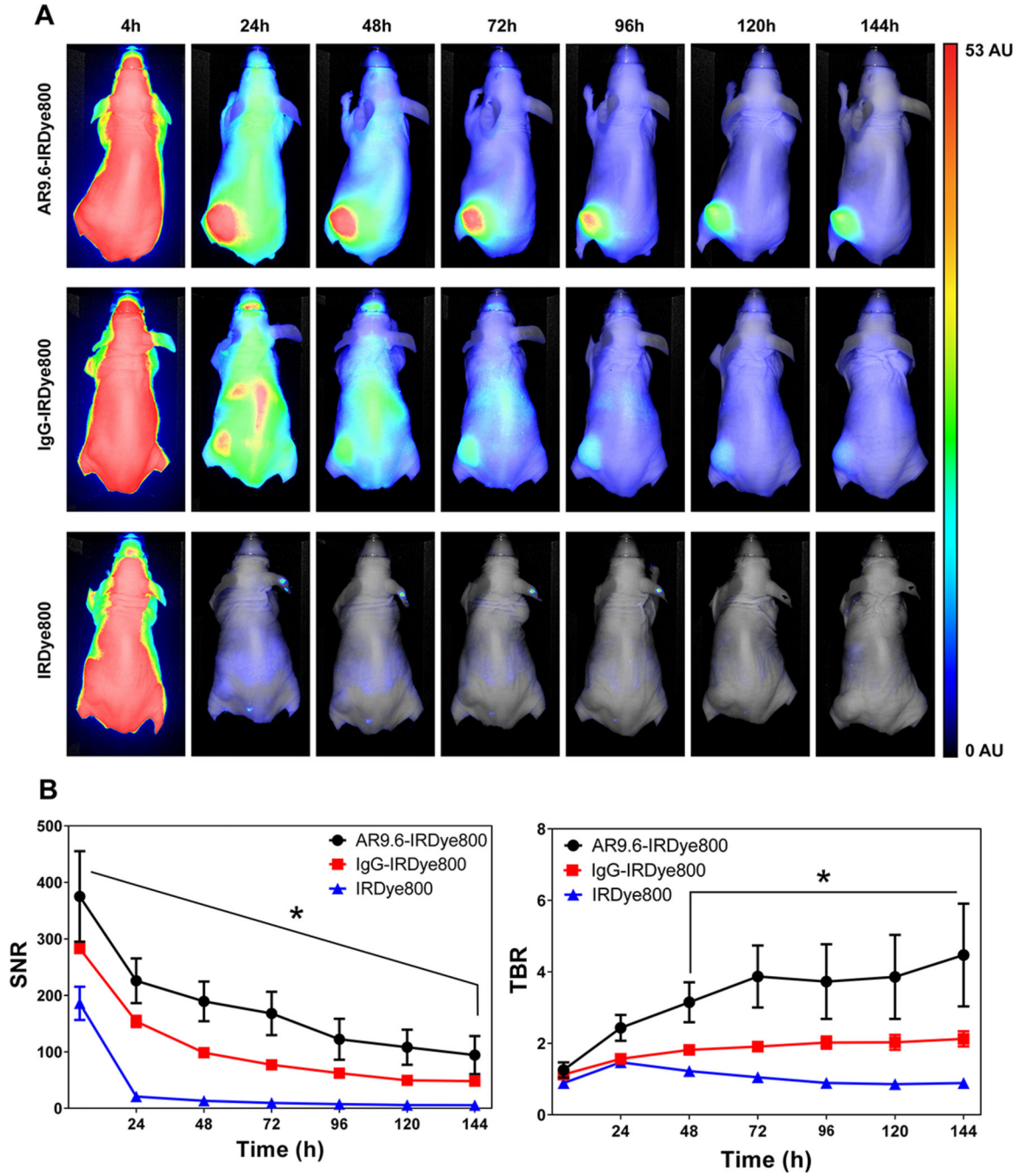

Figure 3.

Tumor accumulation of fluorescent antibody conjugates. (A) Representative images from the biodistribution of the fluorescent conjugates AR9.6-IRDye800, IgG-IRDye800, and unconjugated IRDye800, from 4 −144 h (N = 4). Normalized arbitrary units (AU) depicted on the color bar is representative of all images. (B) Signal to noise ratios and tumor to background ratios of AR9.6-IRDye800, IgG-IRDye800, and unconjugated IRDye800 over 144 h.

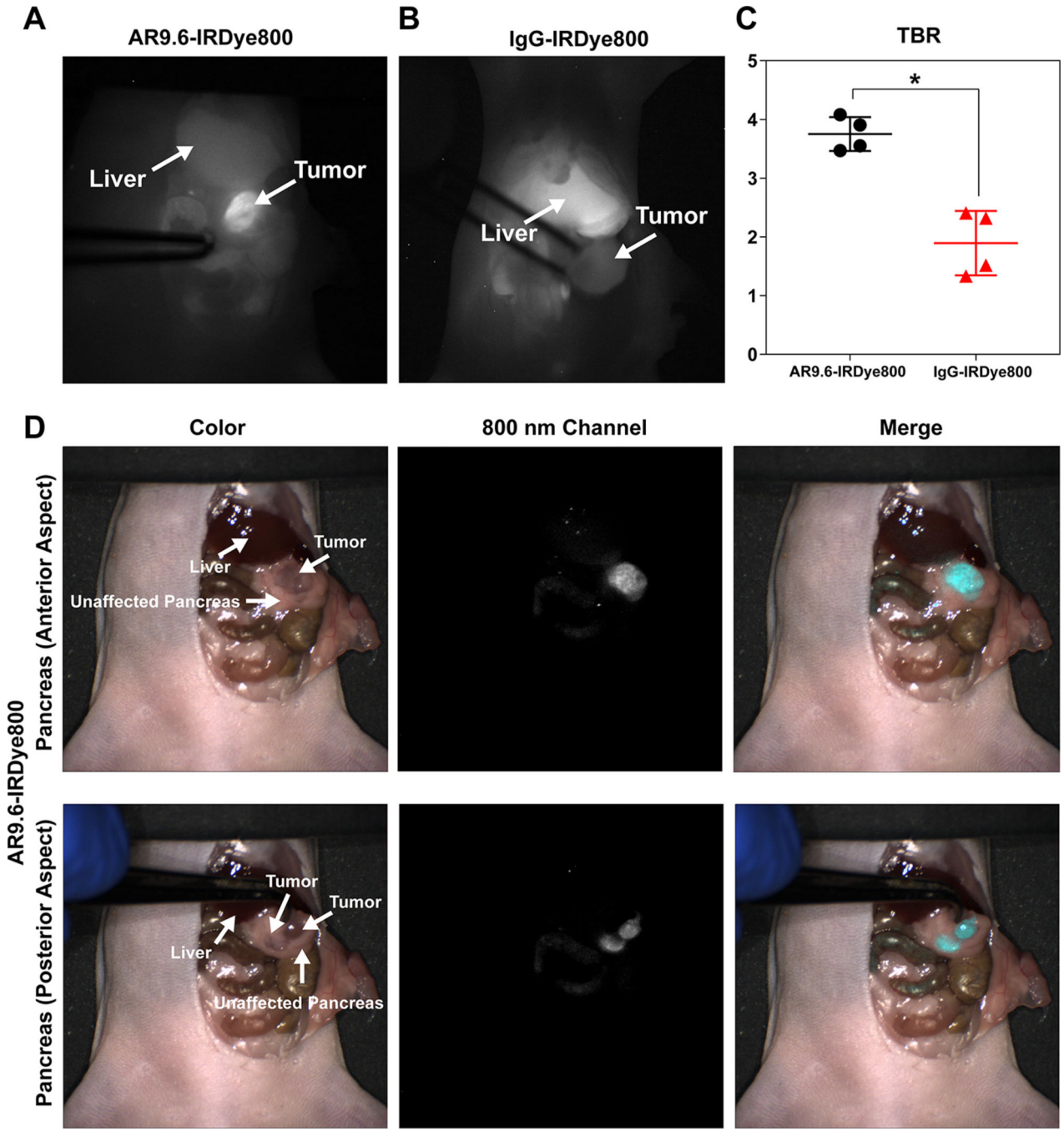

Figure 4.

Fluorescence-Guided Surgery in orthotopic pancreatic cancer. Representative Fluobeam images of FGS with (A) AR9.6-IRDye800 and (B) IgG-IRDye800. (C) Calculated TBR (tumor signal/ adjacent normal pancreas or adjacent peritoneal tissue) in tumors ($p = 0.0010$). (D) Representative images of anterior and posterior pancreas imaging with AR9.6-IRDye800 using the Lab Flare RP1.

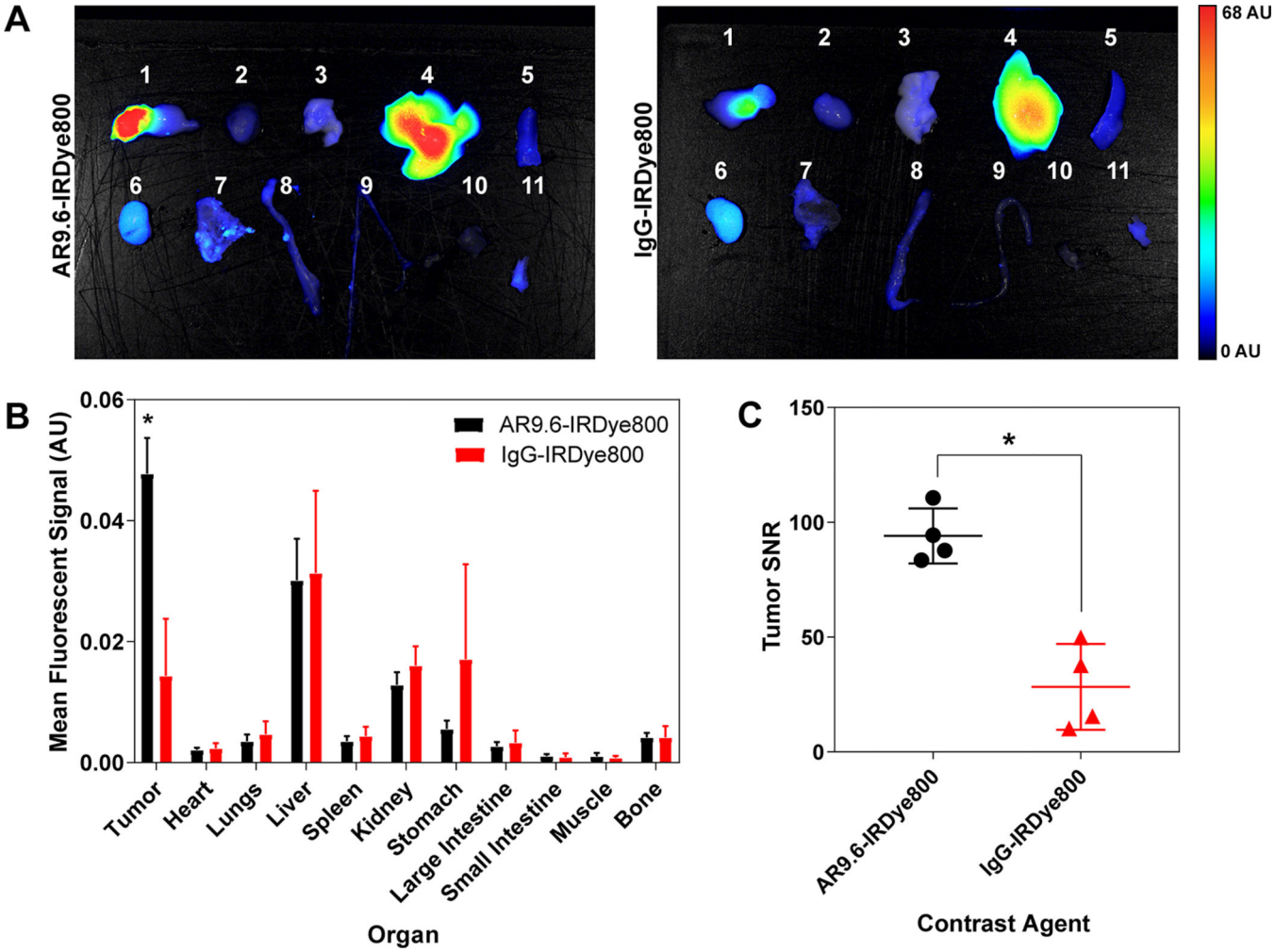

Figure 5.

Biodistribution and signal of AR9.6-IRDye800 and IgG-IRDye800 in an orthotopic xenograft model. (A) Biodistribution of AR9.6-IRDye800 and IgG-IRDye800 at 144 h post-injection in necropsied organs. (*N*=4)) 1=Tumor and Unaffected Pancreas, 2=Heart, 3=Lung, 4=Liver, 5=Spleen, 6=Kidney, 7=Stomach, 8=Large Intestine, 9=Small Intestine, 10=Muscle, 11=Bone. (B) Mean fluorescent signal across necropsied organs. (p = 0.00095) (C) Calculated SNR (tumor signal/ standard deviation of background) in tumors (p = 0.0010).

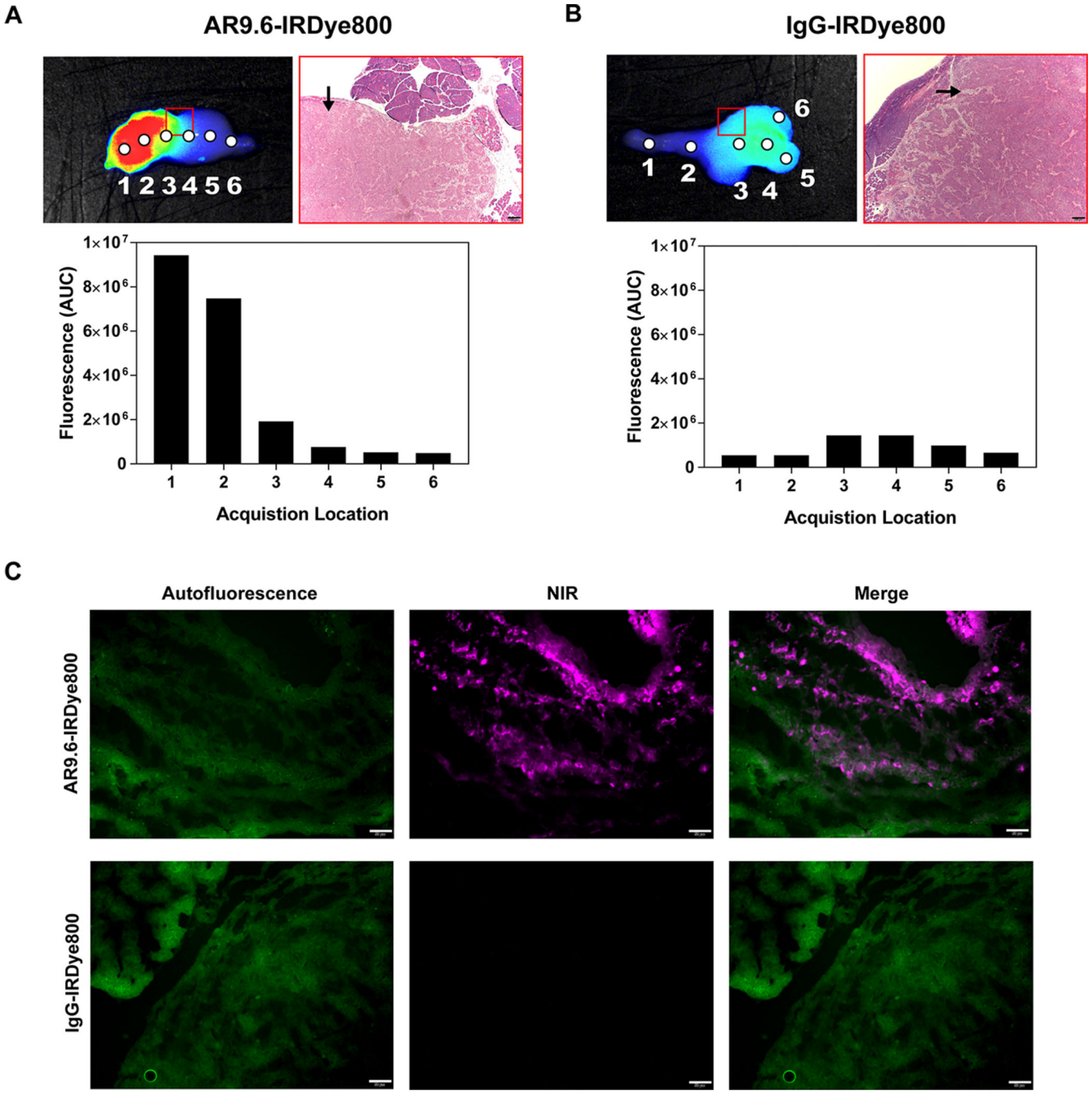

Figure 6.

Spectral analysis of tumors and fluorescent histology. (A) Pearl® Trilogy imaging, H&E staining, and acquired spectra for AR9.6-IRDye800 tumor. The red box denotes the area depicted by the H&E image, and the black arrow denotes tumor. (B) Pearl® Trilogy imaging, H&E staining and acquired spectra for IgG-IRDye800 tumor. (C) Fluorescence microscopy in tumors. Images acquired at 200X magnification. Scale bars = 50 μm.

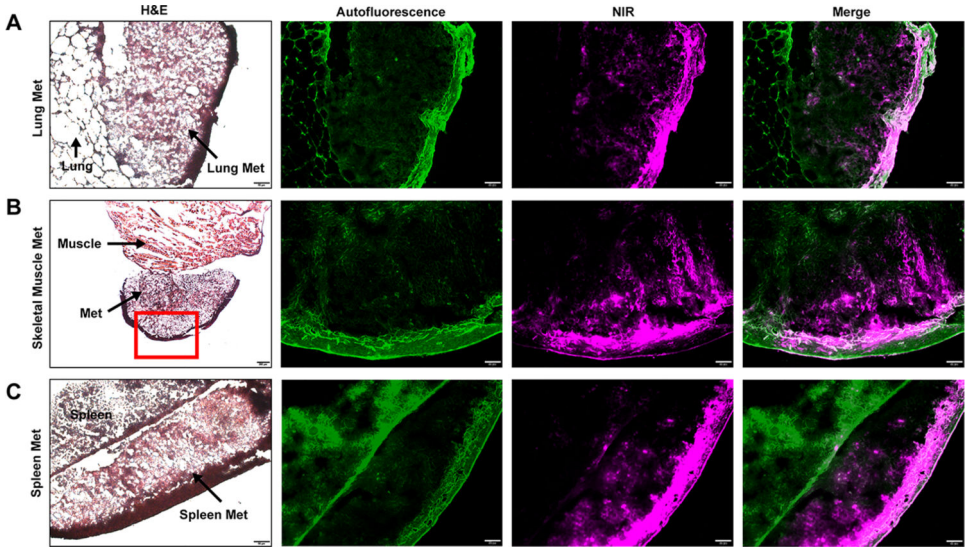

Figure 7.

Identification of micro-metastases. OCT embedded (A) lung metastasis, (B) skeletal muscle metastasis, and (C) spleen metastasis. Images acquired at 200X magnification. Scale bar = 20 μm. Skeletal muscle H&E image acquired at 40X magnification. Scale bar = 200 μm.